Electronic Supplementary Material (ESI) for Journal of Materials Chemistry C.

Supplementary Information

Density functional theory calculations

Density functional theory (DFT) calculations were done on $BaZrO_3$ and $BaCeO_3$ cells with 12.5% yttrium doping. A dopant concentration of 12.5% was used instead of 10% in order to maintain electroneutrality within the cell which had a size of 8 units (2 x 2 x 2). Bond energies were calculated for Ba-O, Zr-O, and Y-O within the BZY system and Ba-O, Ce-O, and Y-O within the BCY system. All DFT calculations were carried out using the plane-wave pseudopotential method as implemented by the Vienna Ab-Initio Simulation Package (VASP)[1–4]. For this study, plane waves with an energy cutoff of 500 eV were constructed using projector augmented wave (PAW) potentials.[5] The generalized gradient approximation (GGA) was applied using the PW91 exchange correlation functional. A 6 x 6 x 6 Monkhorst-Pack sampling of the Brillouin zone was utilized for all calculations[6].

APT sample preparation

Atom probe specimens were prepared from the bulk BZY10 samples using a FEI Helios NanoLab™ 600i focused ion beam (FIB) microscope using a standard wedge lift-out technique and annular milling patterns from the centers of each pellet (to avoid surface contamination/changes).[7] The specimens were mounted with Pt deposition from the FIB onto a copper 200 mesh grid, which had been cut in half and each post pre-thinned using the FIB.[8] Initially, tips were sharpened using a 30 kV Ga-ion beam and then subsequently cleaned with a 2.0 kV Ga-ion beam to minimize Ga damage to the surface. The specimens were inserted in a TEM/APT compatible holder that allowed for analysis on the TEM for imaging and the atom probe for elemental characterization.[8,9] TEM analysis was performed on a 200 kV Phillips CM200 with a 1024 x 1024 CCD detector. All micrographs were collected under an all-beams condition. Fig. S1 shows a FIB lift-out lamella and the close proximity of each tip.

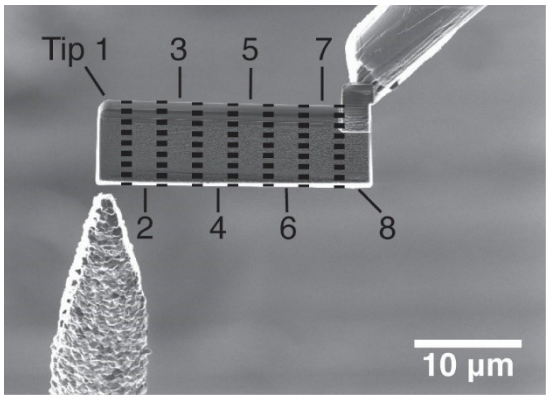

Fig. S1. FIB lift-out lamella of BZY10 SSR-Ni sample showing the close proximity of APT tips. The dashed black lines represent approximately where the lamella was cut once the tips were mounted with Pt to the Cu posts.

Sample preparation for the laser energy optimization

The $BaZr_{0.9}Y_{0.1}O_{3-\delta}$ (BZY10) sample was prepared using spark plasma sintering (SPS) to ensure a dense pellet. First, pure phase BZY10 powder was synthesized via solid-state reaction with $BaCO_3$ (Aldrich 99+%), ZrO_2 (Aldrich, 99.9%), and Y_2O_3 (Sigma-Aldrich, 99.99%) mixed in stoichiometric proportions and ball milled for 20 h. After drying, the mixture was calcined at 1400 °C for 24 h (150 °C/h). The pure powder (no binder) was set in a graphite die and sintered under vacuum using a Sumitomo SPS 2080. Sintering conditions were 1700 °C for 5 min under a load of 100 MPa. A heating rate of 150 °C/min was maintained along with a cooling rate of 100 °C/min down to 800 °C.

The $BaCe_{0.2}Zr_{0.7}Y_{0.1}O_{3-\delta}$ (BCZY27) sample was prepared as a thin film membrane supported by a BCZY27 and NiO anode. Reactant oxide powders $BaSO_4$ (Solvay N grade), CeO_2 (Neo Performance Materials, ≥ 99.5%), ZrO_2 (Neo Performance Materials, ≥ 99.5%), Y_2O_3 (HJD Intl. 99.99+%), and NiO (Inco F grade) were blended with the nominal BCZY27 stoichiometry plus 65 wt. % NiO followed by ball milling for 24 h with deionized water and Duramax™ D-3005 Polymer dispersant (Dow Chemical Co.). The slurry was air dried and sieved through a 40-mesh screen. 2 wt. % of a polyalkylene polyamine polymer binder was added along with Darvan® 821A (R.T. Vanderbilt Co.) to control the viscosity. Tubes 450 mm long with a 14 mm outer diameter and 650 µm wall thickness were slip cast. The green tubes were then dried outside of the molds for 24 h followed by polishing down to a 6 µm finish. Tubes were spray-

coated with a BCZY27 membrane film using a solution containing 50 % solids loading of BCZY27 powder. The coated tubes were dried and fired in an upright arrangement at 1585 °C for 6 h followed by cooling at 100 °C/h. The resulting parts were fully dense membrane and support tubes. After in-situ reduction, the result was a dense hermetic BCZY27 membrane on a porous BCZY27-Ni cermet support.

Both samples were tested in 5 % H_2 in N_2, p(H_2O)) = 0.030 atm) from 600 °C to 200 °C and brought down to room temperature in the same environment, making the materials fully hydrated for APT testing.

Laser energy optimization

Fig. S2 and Fig. S3 show the mass spectra for the BZY10 (Fig. S2) and BCZY27 (Fig. S3) samples at varying laser energy values from 0.1 to 100 pJ. The mass spectra are normalized to the O_2^+ (32 Da peak). It can be seen that the hydrogen peaks (1, 2, and 3 Da) and water peaks (17 and 18 Da) increase with increasing laser energy, suggesting that the higher laser energy causes more hydrogen and water to be field evaporated from the specimen tip. This observation is significant because it shows that it is likely not possible (at least with current APT analysis approaches) to directly measure protons in solid solution in these perovskites because the background hydrogen/water signal is too high, and measured specimen-to-specimen variations may be due primarily to changes in the relative contribution of the laser energy rather than intrinsic compositional differences. With increasing laser energy, the tails of the major peaks (O_2^+, YO^+/ZrO^+, and Ba^{++}) extend to higher Da. This is commonly observed in poor thermal conductors, and is attributed to delayed thermal evaporation of ions after the laser event pulse caused by the slower thermal transport in these highly refractory materials[10–12]. Finally, it can be seen that the preferred ion charge state decreases (for example from ZrO^{++} to ZrO^+ shown in Fig. S5) with increasing laser energy. This observation is also consistent with previous APT studies of ceramics[10,12,13] and is attributed to the dynamic between the laser energy and the standing DC bias. The higher DC bias (and hence higher field strength) required to maintain a constant

detection rate at lower laser energies enhances the probability for field evaporation of higher charge states[14]. Trends in the mass spectra for the BZY10 and BCZY27 samples as a function of laser energy are generally similar, although the greater number of overlapping peaks in the BCZY27 spectra (due to the additional cation) make deconvolution more difficult. This issue is particularly apparent, e.g., in the disappearance of the CeO_2^{++} (86 Da) peak at the highest laser energies due to the large thermal tails of the CeO^{++} (78 Da) and Ba^{++} (68 Da) peaks. Both BZY10 and BCZY27 show the narrowing of peak width with increasing laser energy, which translates to increased mass resolving power (MRP) with increasing laser energy.

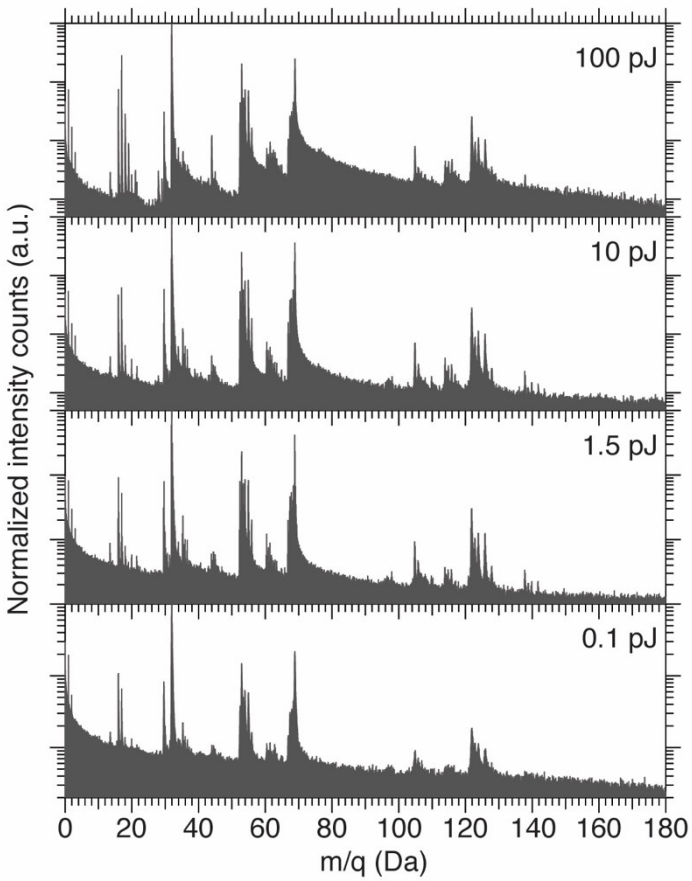

Fig. S2. Mass spectra of the BZY10 specimens obtained at different laser energies showing the changes in field evaporation with larger peak tails due to evaporation after the pulse. The counts were normalized to the intensity of the O_2^+ (32 Da) peak and are without background correction.

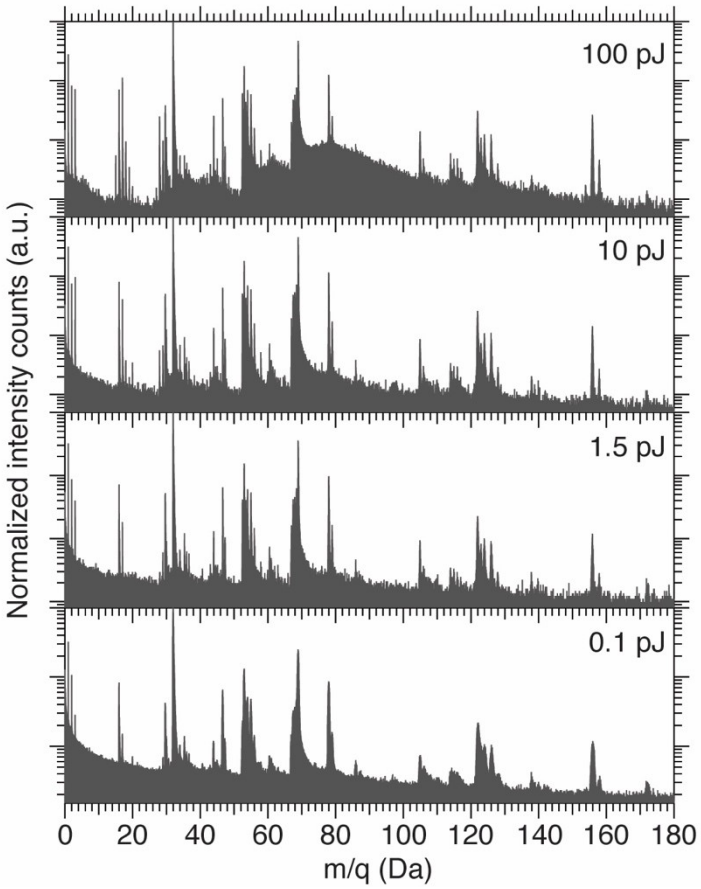

Fig. S3. Mass spectra of the BCZY27 specimens obtained at different laser energies showing the changes in field evaporation with larger peak tails due to evaporation after the pulse. The counts were normalized to the intensity of the O_2^+ (32 Da) peak and are without background correction.

APT data acquisition

APT was performed in a Cameca LEAP 4000X Si system equipped with a 355 nm wavelength laser with a spot size less than 1 µm at full-width half-maximum (FWHM). An optimized laser energy of 10 pJ was used with a pulse frequency of 625 kHz and a specimen base temperature of 40 K.

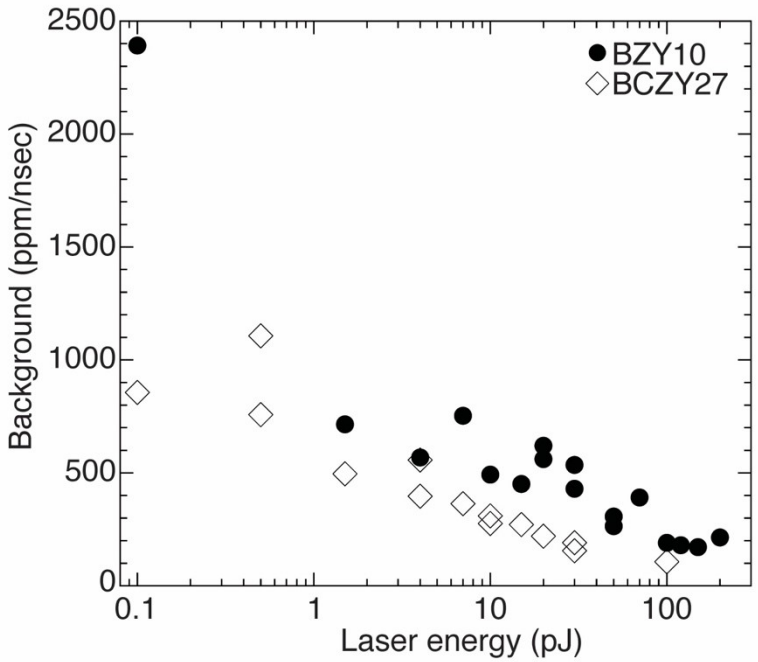

Fig. S4. Mass-spectrum background as a function of laser energy for BZY10 and BCZY27 with more evaporation between pulses at lower laser energies.

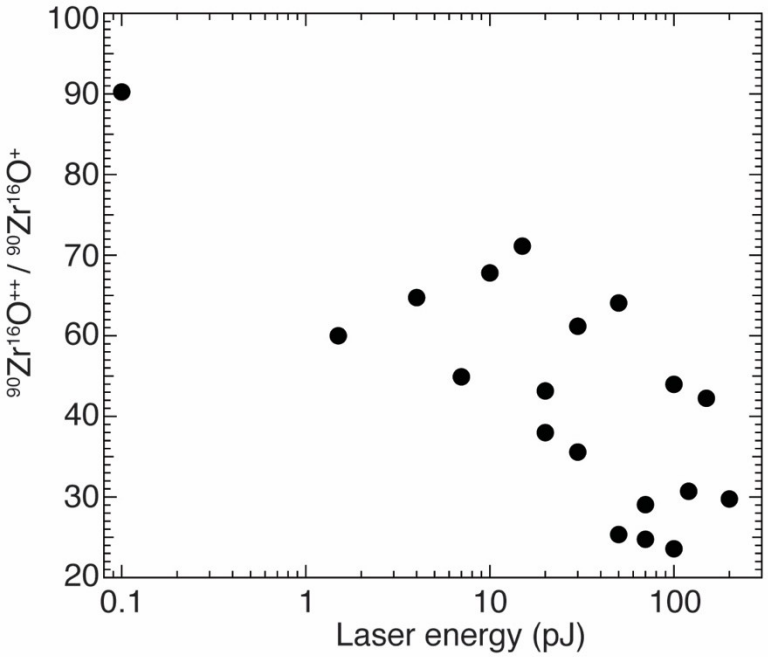

Fig. S5. Charge state ratio of $^{90}Zr^{16}O^{++}/^{90}Zr^{16}O^{+}$ for BZY10 decreasing as a function of laser energy due to lower applied bias.

Data analysis was performed using Cameca's IVAS™ v.3.6.6 software. After ranging the mass spectra and background correcting, 3D reconstructions were made using the tip profile function in IVAS, which uses a TEM micrograph of the tip to complete the reconstruction.[33] This tip profile method inputs the actual tip shape to define the radial evolution of the volume, allowing for more accurate reconstructions. The image compression factor (ICF) and the detection efficiency (DE) were then optimized to give a tip shape that best matched the dimensions obtained from the before and after TEM micrographs (not all APT runs had post-TEM micrographs due to sample failure during the experiment). Differing sphere-to-cone ratios (fixed ratio – FR) were used, obtained from the post-TEM micrographs if available, and correcting for the tangential discontinuity of the specimen tip during evaporation.[34] Table S1 shows the FR, DE, and ICF parameters used for atom probe reconstructions to obtain the best tip shapes corresponding with the TEM micrographs.

For compositional analysis, the highest three peaks were ranged at full-width tenth-maximum (FWTM) of the peak (the intensity of each peak was determined, and the upper and lower bounds were ranged at 10 % of the maximum counts). For BZY10, these peaks were Ba^{++}, ZrO^{++}, and O_2^{+}. The other peaks in the mass spectra were ranged manually to just above background levels. 17 Da OH^{+} was assumed to be water contamination from within the chamber, and, along with other hydrogen and water signals (1, 2, 3, and 18 Da), was ignored. Proton conducting oxides contain bulk hydrogenic (protonic) defects. However, even if the samples are assumed to be fully protonated, the bulk proton concentration is negligible compared to external hydrogenic contamination signals. Oxide stoichiometry was determined using the decomposition-of-peaks method to account for overlapping peak tails. Major peaks which had overlapping tails included $^{89}Y^{+++}/^{90}Zr^{+++}$, $^{16}O_2^{+}/^{90}Zr^{16}O^{+++}$, $^{89}Y^{16}O^{++}/^{90}Zr^{16}O^{++}$, and $^{89}Y^{16}O^{+}/^{90}Zr^{16}O^{+}$. Software-based background correction was accomplished using the local mass-based correction algorithm.

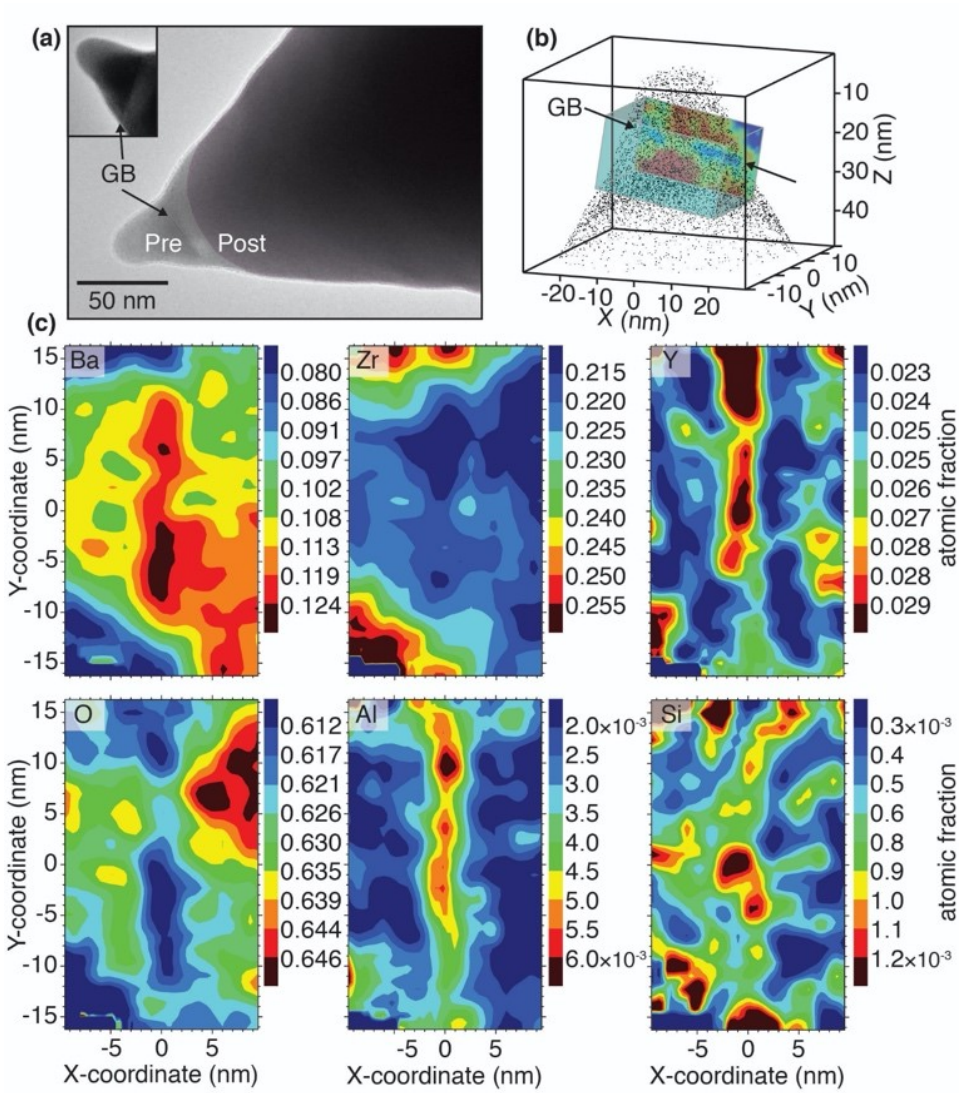

Fig. S6. APT analysis of SPS1. (a) Transmission electron microscopy (TEM) micrographs pre- and post-APT analysis (inset shows more detailed view of GB). (b) Region of interest (ROI) used for (c) elemental atomic fraction 2-D contour maps of Ba, Zr, Y, O, Al, and Si.

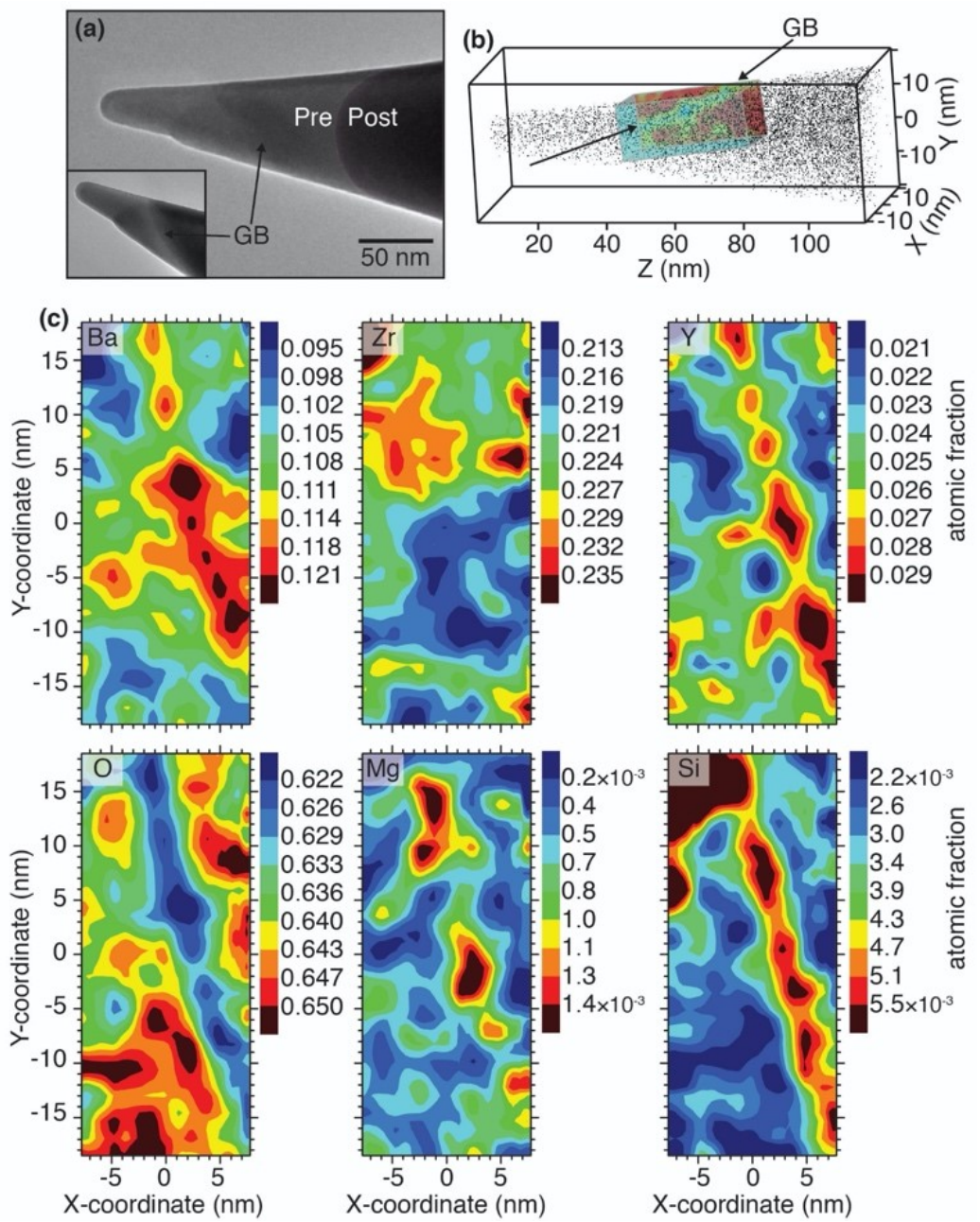

Fig. S7. APT analysis of HT2. (a) Transmission electron microscopy (TEM) micrograph pre-APT analysis. (b) Region of interest (ROI) used for (c) elemental atomic fraction 2-D contour maps of Ba, Zr, Y, O, Al, Mg, Si and Sr.

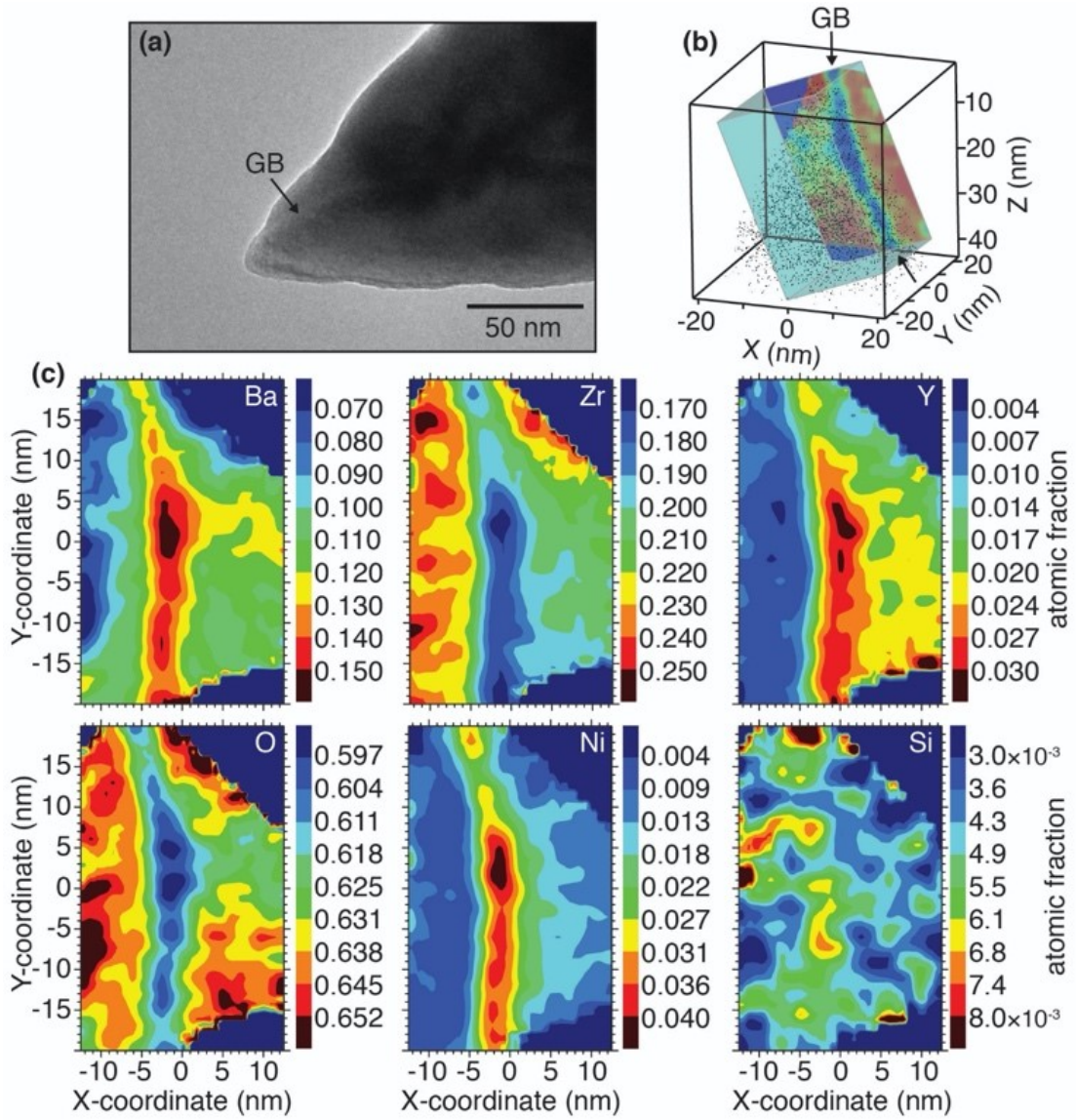

Fig. S8. APT analysis of SSR-Ni2. (a) Transmission electron microscopy (TEM) micrograph pre-APT analysis. (b) Region of interest (ROI) used for (c) elemental atomic fraction 2-D contour maps of Ba, Zr, Y, O, Ni, and Si.

Table S1. List of reconstruction parameters used for each specimen listing the fixed ratio (FR), detector efficiency (DE), and image compression factor (ICF). These parameters were optimized to give the best tip shape to match pre- and post-TEM micrographs of the specimens.

Specimen	FR	DE	ICF
SPS1	1.44	0.40	2.70
SPS2	1.40	0.45	2.00
HT1	1.20	0.45	1.60
HT2	1.15	0.45	1.50
HT3	1.70	0.45	1.60
SSR-Ni1	1.37	0.37	1.35
SSR-Ni2	1.50	0.40	1.55
SSRS-Ni	1.41	0.40	1.52

In addition to the peak overlaps between the major constituents in BZY10, peak overlaps involving the impurity species occur for AlO, Fe, FeO, Ni, Si, SiO, SiO_2, Zr, and ZrO. These overlaps are summarized in Table S2. Peak decomposition applies the expected isotopic ratios of each ionic species to calculate the percent of each overlapping peak that belongs to that species. This fraction of each peak was then taken into account in the contour maps by assigning fractional ranges to the overlapping peaks corresponding to peak decomposition analysis. In order to quantify the average GB versus bulk chemistry, regions of interest (ROI) were picked at the grain boundary (using iso-concentration surfaces if the GB possessed curvature, or a rectangle if the GB was flat). The mass spectra were analyzed and deconvoluted using IVAS deconvolution software, taking into account the overlapping species found in Table S1. Fig. S6 shows an example of a GB ROI where a Ni isoconcentration surface is used to target the GB. Mass spectra were analyzed and decomposed inside and outside of the GB ROI.

Table S2. List of impurities found within the BZY10 specimens which overlap and their corresponding mass-to-charge ratios (m/q). No overlap is shown for isotopic abundances below 4.5 %.

m/q (Da)	Ionic Species
28	$^{28}Si^{+}/^{56}Fe^{++}/^{86}Sr^{+++}$
29	$^{29}Si^{+}/^{58}Ni^{++}$
30	$^{28}Si^{16}O_2^{++}/^{60}Ni^{++}/^{90}Zr^{+++}$
36	$^{56}Fe^{16}O^{++}/^{92}Zr^{16}O^{+++}$
43	$^{27}Al^{16}O^{+}/^{86}Sr^{++}$
44	$^{28}Si^{16}O^{+}/^{88}Sr^{++}$

Chemical analysis of Ni particles in SSRS-Ni grain boundary

Ni-rich particles were found at the GB of the SSRS-Ni sample. Analysis of the chemical composition of the Ni-rich particles was completed using peak decomposition analysis. As shown in Figure S8, these Ni-rich particles appear to have a NiO core, containing some Zr. Fig. S9 is an average proxigram for all of the particles and was calculated using a separate range file, removing species not found in the individual particle mass spectra. Because of this, the proxigram does not correspond to the contour map found in Figure 6c as it is not possible to have a different range file for separate regions when exporting the contour data.

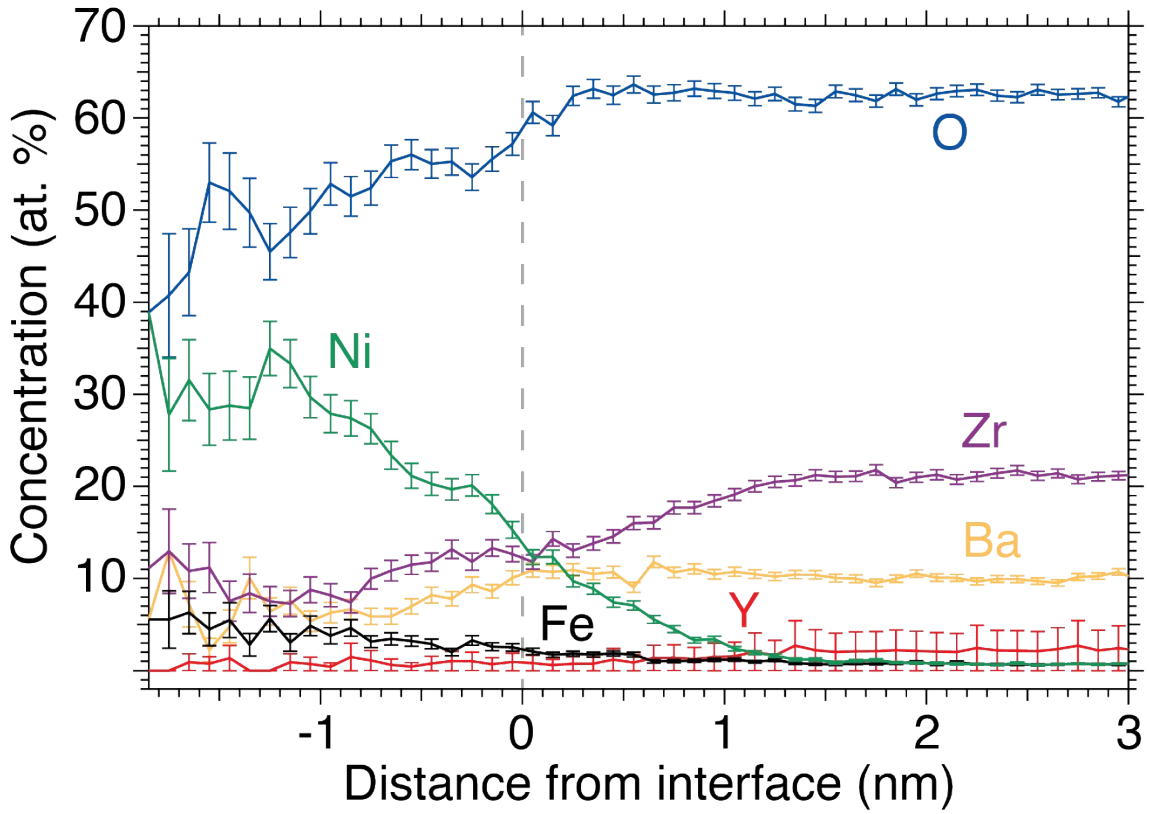

Figure S9. Average proxigram of species concentration as a function of distance from the particle interface. This proxigram was computed from the average of all particles.

Impurities reported in precursors and electrical properties

Impurities are common in the precursors used for BZY material synthesis. Table S3 shows a summary of the precursors used in this study that contain impurities in concentration above 0.001 at. %. Not all manufacturers report impurities.

Table S3. List of impurities found within the precursors used to synthesize the BZY10 samples examined in this study as reported by the manufacturer. Impurities below 0.001 at % are not reported.

Precursor	Impurity Species	Impurity Concentration (at. %)
$BaCO_3$ (Sigma- Aldrich, 99 + %)	Sr	≤ 0.7
	Ca	≤ 0.05
	Na	≤ 0.02
	K	≤ 0.005
	Fe	≤ 0.002
$BaCO_3$ (Alfa Aesar, 99.95%)	Sr	≤ 0.012
NiO (Novamet, Inco F-Grade)	Fe	≤ 0.015
	Al	≤ 0.005
	Si	≤ 0.005
	Co	≤ 0.0015
ZrO_2 (Tosoh, 99.9%)	Al	≤ 0.1
	Na	≤ 0.01

Table S4. Summary of properties of all SPS, HT, SSR-Ni, and SSRS samples obtained from Ricote et al. of synthesis method, sintering temperature, total conductivity at 600 and 500 °C, R_{GB}/R_{bulk}, bulk, and GB activation energy, electrical barrier height at the GB (ϕ), and grain size.[9]

Synthesis	Sintering Temp (°C)	Total conductivity (mS/cm)		R_{GB}/R_{bulk}	$E_{a,bulk}$ (eV)	$E_{a,sp.GB}$ (eV)	Φ (V)	Grain Size (um)
		600 °C	500 °C					
SPS	1700	2.32	1.4	7.4	0.39	0.77	0.17	0.3-0.8
HT	2200	3.43	1.7	5.6	0.42	0.69	0.15	1-10
SSR-Ni	1600	2.7	1.1	12.6	0.40	0.84	0.20	1-4
SSRS-Ni	1535	3	1.6	1.1	0.39	0.45	0.04	1-6

The values reported in Fig. 10 can be found below in Table S5 and Table S6.

Table S5. Summary of [GB]/[bulk] ratio for the SPS, HT, SSR, and SSRS specimens.

	[GB]/[bulk]			
Specimen	**Ba**	**Zr**	**Y**	**O**
SPS1	1.17 ± 0.02	0.95 ± 0.01	1.12 ± 0.04	0.97 ± 0.01
SPS2	1.15 ± 0.02	0.98 ± 0.01	1.30 ± 0.04	0.97 ± 0.01
HT1	1.33 ± 0.02	0.98 ± 0.01	1.10 ± 0.03	0.95 ± 0.01
HT2	1.27 ± 0.03	0.98 ± 0.01	1.25 ± 0.04	0.95 ± 0.01
HT3	0.62 ± 0.08	1.25 ± 0.02	0.84 ± 0.01	0.94 ± 0.01
SSR-Ni1	1.40 ± 0.06	0.83 ± 0.01	2.17 ± 0.14	0.92 ± 0.01
SSR-Ni2	1.42 ± 0.03	0.83 ± 0.01	1.83 ± 0.06	0.9 ± 0.01
SSRS-Ni	0.56 ± 0.04	0.84 ± 0.01	1.43 ± 0.06	0.96 ± 0.01

	[GB]/[bulk]					
Specimen	**Al**	**Fe**	**Mg**	**Ni**	**Si**	**Sr**
SPS1	3.10 ± 0.32	2.61 ± 0.59	0.10 ± 0.01	-	0.92 ± 0.12	0.74 ± 0.32
SPS2	3.54 ± 0.33	1.44 ± 0.27	1.81 ± 0.41	-	1.19 ± 0.06	3.76 ± 2.36
HT1	6.39 ± 3.44	1.62 ± 0.99	15.36 ± 6.65	-	1.89 ± 0.61	6.39 ± 8.29
HT2	2.25 ± 0.29	8.88 ± 9.40	0.87 ± 0.44	-	7.54 ± 0.71	0.78 ± 1.93
HT3	17.2 ± 11.4	7.66 ± 6.98	2.42 ± 5.23	-	47.93 ± 6.55	3.31 ± 1.66
SSR-Ni1	1.66 ± 0.39	1.58 ± 0.29	-	7.57 ± 1.4	1.67 ± 0.13	2.89 ± 5.95
SSR-Ni2	0.65 ± 0.06	1.04 ± 0.19	-	6.30 ± 0.38	0.56 ± 0.07	5.79 ± 8.49
SSRS-Ni	13.48 ± 1.86	5.24 ± 1.68	-	57.26 ± 5.46	10.05 ± 1.97	1.72 ± 0.15

Table S6. Summary of grain boundary concentrations (at. %) for the SPS, HT, SSR, and SSRS specimens.

	Grain boundary concentration (at. %)			
Specimen	**Ba**	**Zr**	**Y**	**O**
SPS1	11.79 ± 0.22	22.94 ± 0.07	2.88 ± 0.07	62.20 ± 0.09
SPS2	10.95 ± 0.16	22.02 ± 0.08	2.36 ± 0.05	63.48 ± 0.05
HT1	12.23 ± 0.16	22.30 ± 0.07	3.09 ± 0.06	61.25 ± 0.06
HT2	11.85 ± 0.24	22.43 ± 0.14	2.87 ± 0.08	62.41 ± 0.09
HT3	8.22 ± 0.74	27.48 ± 0.21	2.46 ± 0.26	60.13 ± 0.40
SSR-Ni1	14.82 ± 0.37	18.38 ± 0.05	2.48 ± 0.09	60.47 ± 0.12
SSR-Ni2	14.10 ± 0.19	18.94 ± 0.06	2.81 ± 0.06	60.35 ± 0.07
SSRS-Ni	9.00 ± 0.22	20.91 ± 0.06	2.47 ± 0.09	61.91 ± 0.12

	Grain boundary concentration (at. %)					
Specimen	**Al**	**Fe**	**Mg**	**Ni**	**Si**	**Sr**
SPS1	0.55 ± 0.04	0.81 ± 0.08	0.05 ± 0.01	-	0.10 ± 0.01	0.33 ± 0.13
SPS2	0.49 ± 0.03	0.35 ± 0.06	0.04 ± 0.01	-	0.40 ± 0.02	0.14 ± 0.08
HT1	0.11 ± 0.03	0.12 ± 0.05	0.19 ± 0.03	-	0.19 ± 0.02	0.20 ± 0.04
HT2	0.12 ± 0.01	0.24 ± 0.09	0.13 ± 0.01	-	0.54 ± 0.05	0.02 ± 0.02
HT3	0.06 ± 0.03	0.35 ± 0.03	0.01 ± 0.02	-	0.45 ± 0.02	0.25 ± 0.12
SSR-Ni1	0.12 ± 0.03	0.67 ± 0.07	-	4.00 ± 0.22	0.60 ± 0.05	0.08 ± 0.13
SSR-Ni2	0.13 ± 0.01	0.28 ± 0.04	-	3.43 ± 0.12	0.50 ± 0.03	0.11 ± 0.16
SSRS-Ni	0.36 ± 0.04	1.39 ± 0.41	-	3.48 ± 0.15	0.96 ± 0.21	1.14 ± 0.12

References

1 G. Kresse and J. Hafner, *Phys. Rev. B*, 1993, **47**, 558–561.

2 G. Kresse and J. Hafner, *Phys. Rev. B*, 1994, **49**, 14251–14269.

3 G. Kresse and J. Furthmüller, *Comput. Mater. Sci.*, 1996, **6**, 15–50.

4 G. Kresse, *Phys. Rev. B*, 1996, **54**, 11169–11186.

5 J. P. Perdew, K. A. Jackson, M. R. Pederson, D. J. Singh and C. Fiolhais, *Phys. Rev. B*, 1992, **46**, 6671–6687.

6 H. J. Monkhorst and J. D. Pack, *Phys. Rev. B*, 1976, **13**, 5188–5192.

7 K. Thompson, D. Lawrence, D. J. Larson, J. D. Olson, T. F. Kelly and B. Gorman, *Ultramicroscopy*, 2007, **107**, 131–139.

8 B. P. Gorman, D. Diercks, N. Salmon, E. Stach, G. Amador and C. Hartfield, *Micros. Today*, 2008, **16**, 42–47.

9 B. Gorman, D. Diercks and D. Jaeger, *Microsc. Microanal.*, 2008, **14**, 1042–1043.

10 R. Kirchhofer, M. C. Teague and B. P. Gorman, *J. Nucl. Mater.*, 2013, **436**, 23–28.

11 R. Agrawal, R. A. Bernal, D. Isheim and H. D. Espinosa, *J. Phys. Chem. C*, 2011, **115**, 17688–17694.

12 D. R. Diercks, B. P. Gorman, R. Kirchhofer, N. Sanford, K. Bertness and M. Brubaker, *J. Appl. Phys.*, 2013, **114**, 184903.

13 A. Devaraj, R. Colby, W. P. Hess, D. E. Perea and S. Thevuthasan, *J. Phys. Chem. Lett.*, 2013, **4**, 993–998.

14 D. R. Kingham, *Surf. Sci.*, 1982, **116**, 273–301.